

Elimination of the Blue Loops in the Evolution of Intermediate-mass Stars by the Neutrino Magnetic Moment and Large Extra Dimensions

Kanji Mori^{1,2,6}, A. Baha Balantekin^{2,3}, Toshitaka Kajino^{1,2,4}, and Michael A. Famiano^{2,5} Graduate School of Science, The University of Tokyo, 7-3-1 Hongo, Bunkyo-ku, Tokyo, 113-0033 Japan; kanji.mori@grad.nao.ac.jp

National Astronomical Observatory of Japan, 2-21-1 Osawa, Mitaka, Tokyo 181-8588, Japan

Department of Physics, University of Wisconsin–Madison, Madison, WI 53706, USA

School of Physics, Beihang University, 37 Xueyuan Road, Haidian-qu, Beijing 100083, People's Republic of China

Department of Physics, Western Michigan University, Kalamazoo, MI 49008, USA

Received 2020 April 14; revised 2020 August 17; accepted 2020 August 18; published 2020 September 29

Abstract

For searching beyond Standard Model physics, stars are laboratories that complement terrestrial experiments. Massless neutrinos in the Standard Model of particle physics cannot have a magnetic moment, but massive neutrinos have a finite magnetic moment in the minimal extension of the Standard Model. Large extra dimensions (LEDs) are a possible solution of the hierarchy problem. Both of these provide additional energy-loss channels in stellar interiors via the electromagnetic interaction and radiation into extra dimensions, respectively, and thus affect stellar evolution. We perform simulations of stellar evolution with such additional energy losses and find that they eliminate the blue loops in the evolution of intermediate-mass stars. The existence of Cepheid stars can be used to constrain the neutrino magnetic moment (NMM) and LEDs. In order for Cepheids to exist, the NMM should be smaller than the range $\sim 2 \times 10^{-10} \mu_{\rm B}$ –4 $\times 10^{-11} \mu_{\rm B}$, where $\mu_{\rm B}$ is the Bohr magneton, and the fundamental scale in the (4+2)-spacetime should be larger than ~ 2 –5 TeV, depending on the rate of the $^{12}{\rm C}$ (α , γ) $^{16}{\rm O}$ reaction. The fundamental scale also has strong dependence on the metallicity. This value of the magnetic moment is in the range explored in the reactor experiments, but higher than the limit inferred from globular clusters. Similarly the fundamental scale value we constrain corresponds to a size of the compactified dimensions comparable to those explored in the torsion balance experiments, but it is smaller than the limits inferred from collider experiments and low-mass stars.

Unified Astronomy Thesaurus concepts: Non-standard theories of gravity (1118); Stellar evolution (1599); Cepheid variable stars (218); Neutrino astronomy (1100); Particle astrophysics (96)

1. Introduction

Intermediate-mass stars deviate from the red giant branch and form a loop toward the blue region in the Hertzsprung-Russell (H-R) diagram during central helium burning (Kippenhahn et al. 2012). Such a loop is called a "blue loop." Stars spend considerable time on the blue loop, so many blue giants have been discovered (e.g., Evans 1993; Dohm-Palmer & Skillman 2002; McQuinn et al. 2011). The blue loops can cross the Cepheid instability strip if their endpoints extend to high enough temperature. In that case, the stars on the blue loops are observed as Cepheid variables.

Stars have been used to explore beyond-standard physics that may be difficult to reach with laboratory experiments (Raffelt 1996). Recently, it was pointed out that the blue loops in the evolution of intermediate-mass stars can be eliminated if energy loss from axion emission (Friedland et al. 2013) is included in stellar evolution calculations. Because the blue loops are a ubiquitous characteristic of blue giants and Cepheid variables, this is a powerful way to relate new physics to observations. We apply this idea to the exploration of nonstandard energy losses that originate from the neutrino magnetic moment (μ_{ν} ; NMM) and large extra dimensions (LEDs).

In the Standard Model (SM) of particle physics, neutrinos are assumed to be massless. However, neutrino oscillation observations have revealed that they have mass eigenstates (e.g., Fukuda et al. 1998). The NMM is allowed only for massive neutrinos and the minimally extended SM predicts a

small but finite magnetic moment (Fujikawa & Shrock 1980; Shrock 1982).

Since the NMM is a key to physics beyond the SM, several experiments have been performed to find it and determine its magnitude (Giunti & Studenikin 2015; Balantekin & Kayser 2018). The most recent constraint comes from the GEMMA experiment (Beda et al. 2013), which measures the scattering cross sections of electrons and reactor antielectron neutrinos. This constrains the magnetic moment at $\mu_{\nu} < 2.9 \times 10^{-11} \mu_{\rm B}$ (90% C.L.).

In addition to the intermediate-mass stars considered here, NMMs can also be constrained from low-mass stars. The luminosity of the tip of red giant branch is sensitive to the energy loss. Theoretical luminosities are compared to the color–magnitude diagram of globular clusters (Raffelt & Weiss 1992; Viaux et al. 2013a, 2013b; Arceo-Díaz et al. 2015), and a stringent constraint, $\mu_{\nu} < 2.2 \times 10^{-12} \mu_{\rm B}$, is reported (Arceo-Díaz et al. 2015).

The idea of LEDs is proposed by Arkani-Hamed et al. (1998) and Antoniadis et al. (1998) to solve the hierarchy problem, i.e., the huge difference between the electroweak scale \sim TeV and the Planck scale \sim 10¹⁶ TeV (Tanabashi et al. 2018). The Planck mass $M_{\rm S}$ in the (4 + n)-dimensional spacetime is related to $M_{\rm P}$ in the four-dimensional spacetime as (Barger et al. 1999)

$$M_{\rm P}^2 = \Omega_n R^n M_{\rm S}^{n+2},\tag{1}$$

where R is the size of the compactified dimensions and Ω_n is a numerical factor that depends on the geometry of compactification. For example, for a torus $\Omega_n = (2\pi)^n$. In order for the

⁶ Research Fellow of Japan Society for the Promotion of Science.

hierarchy problem to be solved, $M_{\rm S}$ should coincide with the electroweak scale. For the n=1 model, this requires $R\sim 10^{10}$ km, which is clearly excluded by the inverse-square law on the scale of the solar system. In this study, therefore, we focus on the simplest possible case of $n\geqslant 2$.

The most direct probes of extra dimensions come from torsion balance experiments (Adelberger et al. 2009; Murata & Tanaka 2015), which measure gravitation at the submillimeter range. The gravitational field between two masses m_1 and m_2 is often parameterized by the Yukawa potential

$$V(r) = -G\frac{m_1 m_2}{r} (1 + \alpha e^{-r/R}). \tag{2}$$

The n=2 model corresponds to $\alpha=16/3$. The most recent torsion experiments report $R\leqslant 37~\mu\mathrm{m}$ (Tan et al. 2020) and $R<30~\mu\mathrm{m}$ (Lee et al. 2020). For n=2 this corresponds to a limit of $M_{\mathrm{S}}\gtrsim 3$ TeV. For n=3 this corresponds to a lower limit on M_{S} that is well below the electroweak scale.

Hadron colliders have also been used to search for gravitons. These cannot be directly detected, so energetic jets are examined for missing transverse energy. From this, the value of $M_{\rm D}$ is extracted, where $M_{\rm D}$ is defined as

$$M_{\rm P}^2 = R^n M_{\rm D}^{n+2}.\tag{3}$$

The Compact Muon Solenoid (CMS) experiment at the Large Hadron Collider reports $M_{\rm D} > 9.9$ TeV for n=2 (Sirunyan et al. 2018). This corresponds to a limit of $M_{\rm S} \gtrsim 3.9$ TeV. The corresponding limits from the ATLAS Collaboration are slightly lower (Aaboud et al. 2018).

A more stringent bound comes from γ -ray fluxes from neutron stars (Hannestad & Raffelt 2003; Fermi-LAT Collaboration et al. 2012). A recent observation by the Fermi Large Area Telescope reports a constraint R < 9.5 nm for the n = 2 model (Fermi-LAT Collaboration et al. 2012).

Stellar evolution calculations have shown that the tip of the red giant branch is sensitive to LEDs. Cassisi et al. (2000) conclude that $M_{\rm S}>3$ TeV by comparing stars in globular clusters and theoretical stellar evolution. This value is similar to the experimental bounds coming from collider and torsion experiments. Both types of experiments—with very different systematic errors—yield bounds in $M_{\rm S}$ that are comparable to those derived from evaluations of the tip of the red giant branch.

Similarly, bounds on NMMs obtained from arguments of energy loss in low-mass stars are within an order of magnitude of the experimental bounds. Terrestrial experiments looking for extra dimensions, such as the torsion balance experiments, and those looking for NMMs are reaching their limits of exploration. To improve the limits on the inverse-square law requires a significant increase in the background-free sensitivity for the torsion balance experiments, which will be rather difficult. To improve the limits on the NMM requires the ability to measure an exceedingly small amount of the electron recoil energy. Limits from both kinds of terrestrial experiments are subject to very different systematic errors as compared to the limits from low-mass stars. Hence, it is desirable to explore whether other astronomical test beds can yield limits subject to different systematic errors. In this paper we explore bounds obtained from considerations of evolution of intermediate-mass stars in the "blue loop" epoch, as these would be subject to different uncertainties than the low-mass stars.

This paper is organized as follows. Section 2 describes the treatment of the extra energy loss due to NMMs and LEDs in stellar models. Section 3 describes the results of stellar evolution calculations. In Section 4, we summarize and discuss the constraints achieved in this study.

2. Method

2.1. Energy Loss by the NMM

For a nonzero NMM, the neutrino energy loss increases because of an additional electromagnetic contribution to the neutrino emissivity. Here we consider two processes: plasmon decay $(\gamma \to \nu \bar{\nu})$ and neutrino pair production $(e^+e^- \to \nu \bar{\nu})$. The additional energy-loss rate due to plasmon decay is given as (Haft et al. 1994; Heger et al. 2009)

$$\epsilon_{\text{plas}}^{\mu} = 0.318 \left(\frac{\omega_{\text{pl}}}{10 \text{ keV}} \right)^{-2} \left(\frac{\mu_{\nu}}{10^{-12} \mu_{\text{B}}} \right)^{2} \epsilon_{\text{plas}},$$
(4)

where $\epsilon_{\rm plas}$ is the standard energy loss (Itoh et al. 1996) and $\omega_{\rm pl}$ is the plasma frequency (Raffelt 1996)

$$\omega_{\rm pl} = 28.7 \,\text{eV} \frac{(Y_{\rm e}\rho)^{\frac{1}{2}}}{(1 + (1.019 \times 10^{-6}Y_{\rm e}\rho)^{\frac{2}{3}})^{\frac{1}{4}}}.$$
 (5)

Here Y_e is the electron fraction and ρ is the density in units of g cm⁻³. The additional energy-loss rate due to pair production is written as (Heger et al. 2009)

$$\epsilon_{\text{pair}}^{\mu} = 1.6 \times 10^{11} \,\text{erg g}^{-1} \,\text{s}^{-1} \left(\frac{\mu_{\nu}}{10^{-10}\mu_{\text{R}}}\right)^{2} \frac{e^{-\frac{118.5}{78}}}{\rho_{4}},$$
 (6)

where $T_8 = T/(10^8 \text{ K})$ and $\rho_4 = \rho/(10^4 \text{ g cm}^{-3})$.

2.2. Energy Loss by LEDs

A possible existence of compactified extra dimensions results in Kaluza–Klein (KK) modes of gravitons $G_{\rm KK}$ with mass $m_n^2=n^2/R^2$, where n is the index for the nth KK modes. The KK gravitons can radiate into extra dimensions and thus work as an additional source of the energy loss, while SM particles are confined to the four-dimensional subspace. We consider three processes: photon–photon annihilation $(\gamma\gamma \to G_{\rm KK})$, gravi–Compton-Primakoff scattering $(e^-\gamma \to e^-G_{\rm KK})$ and gravi-brems-strahlung $(e^-(Ze) \to e^-(Ze)G_{\rm KK})$.

The numerical formulae for these processes are given in Hansen et al. (2015) and Barger et al. (1999). The energy-loss rates for photon-photon annihilation, gravi-Compton-Primak-off scattering, and gravi-bremsstrahlung in the nondegenerate condition are given by

$$\epsilon_{\gamma\gamma} = 5.1 \times 10^{-9} T_7^9 \rho_6^{-1} \left(\frac{M_{\rm S} c^2}{1 \text{ TeV}} \right)^{-4} \text{erg g}^{-1} \text{s}^{-1},$$
 (7)

$$\epsilon_{\text{GCP}} = 4.5 \times 10^{-6} T_7^7 \left(\frac{M_{\text{S}} c^2}{1 \text{ TeV}} \right)^{-4} \text{erg g}^{-1} \text{ s}^{-1},$$
 (8)

$$\epsilon_{\rm GB} = 5.8 \times 10^{-3} \bar{Z}_7^2 T_7^3 \left(\frac{M_{\rm S} c^2}{1 \text{ TeV}} \right)^{-4} \text{erg g}^{-1} \text{ s}^{-1},$$
 (9)

respectively. Here \bar{Z}_7 is the mean ion charge relative to nitrogen, $T_7 = T/(10^7 \text{ K})$, and $\rho_6 = \rho/(10^6 \text{ g cm}^{-3})$.

Table 1
The Initial Composition Adopted in Our Models

	X	Y	Z
Case A	0.70	0.28	0.02
Case B	0.7389	0.2463	0.0148

2.3. Stellar Model

We use a one-dimensional stellar evolution code Modules for Experiments in Stellar Astrophysics (MESA; Paxton et al. 2011, 2013, 2015, 2018, 2019) version 10398. The code adopts the equation of state of Rogers & Nayfonov (2002) and Timmes & Swesty (2000) and opacities of Iglesias & Rogers (1996, 1993) and Ferguson et al. (2005). Nuclear reaction rates are taken from NACRE (Angulo et al. 1999), with weak rates from Langanke & Martínez-Pinedo (2000), Oda et al. (1994), and Fuller et al. (1985). The prescription for screening is based on Alastuey & Jancovici (1978) and Itoh et al. (1979).

The initial composition adopted in our models is based on the solar system abundances. Conventionally, the standard solar metallicity has been Z=0.02 (Anders & Grevesse 1989). However, recent literature shows lower metallicities of Z=0.0122 (Asplund et al. 2005), 0.0134 (Asplund et al. 2009) and 0.0148 (Lodders 2020). In our models, we adopt two compositions: (Y, Z)=(0.28, 0.02) from Anders & Grevesse (1989) and (Y, Z)=(0.2463, 0.0148) from Asplund et al. (2009). We call these models Case A and Case B, respectively (Table 1).

Convective mixing lengths are fixed to $\alpha=1.6$, which were adopted in Friedland et al. (2013). The overshoot parameter is set to be $f_{\rm ov}=0.005$. When the effective temperature $T_{\rm eff}$ is lower than 10^4 K, the mass-loss table compiled by de Jager et al. (1988) is used. When $T_{\rm eff}$ is higher than 10^4 K, mass loss is not taken into account. Pulsation-driven mass loss (Neilson & Lester 2008; Neilson et al. 2011) within the Cepheid instability strip is not considered. The nuclear reaction network includes 22 nuclides (approx21_plus_co56.net). Evolution is followed until the end of core helium burning.

3. Results

We calculate nonrotating stellar models with 7, 8, 9, and $10M_{\odot}$.⁷ The adopted NMM is $\mu_{12} = 100$, 200 and 300, where μ_{12} is the NMM in units of 10^{-12} $\mu_{\rm B}$, and the LED adopted mass scales are $M_{\rm S} = 3$, 2, and 1 TeV.⁹ In Section 3.1, we show the H-R diagrams of these models. In Section 3.2, we discuss the evolution of the helium burning core and the contribution of each elementary process to the energy loss.

3.1. Elimination of the Blue Loops

3.1.1. Case A

The top panel of Figure 1 is the H-R diagram for the standard case. In this case, all of the models with $7-10M_{\odot}$ show the blue

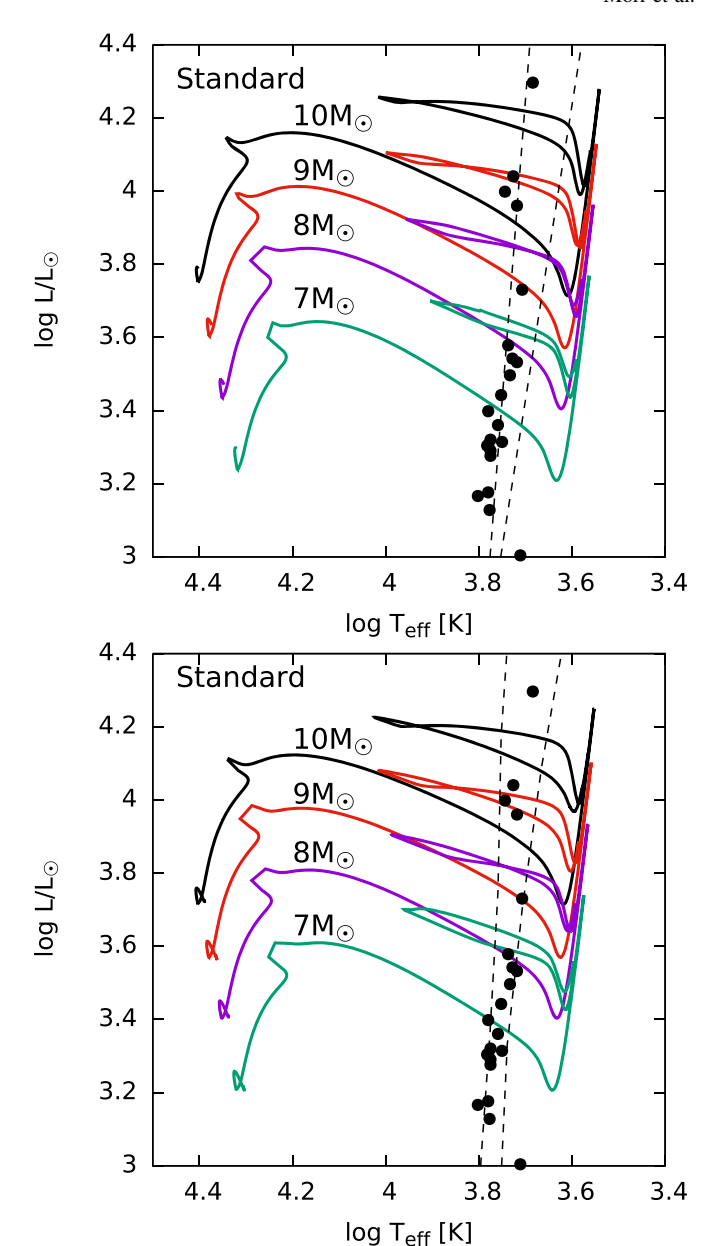


Figure 1. H-R diagram with standard physics. The top panel shows the models with Z=0.02 (i.e., Case A), and the bottom panel shows the models with Z=0.0148 (i.e., Case B). The dashed lines indicate the edges of the instability strip in models. The Z=0.02 models in Bono et al. (2000) are adopted for Case A, and the Z=0.014 model in Anderson et al. (2016) is adopted in Case B. The points are samples of Galactic Cepheids reported in Turner & Burke (2002).

loops. The loops in this mass range cross the Cepheid instability strip, in which stars pulsate as Cepheid variables.

Figure 2 is the H-R diagram of stars with NMMs of $\mu_{12} = 100$, 200, and 300. Though the morphology of the blue loops does not change when $\mu_{12} = 100$, in the case of $\mu_{12} = 200$ the loop is eliminated for the $10M_{\odot}$ star. When the NMM is as large as $\mu_{12} = 300$, only the $7M_{\odot}$ model exhibits a blue loop, while its morphology is significantly affected.

Figure 3 shows H-R diagrams of stars with LEDs of $M_{\rm S}=3$, 2, and 1 TeV. It is seen that, when $M_{\rm S}=3$ TeV, the blue loops remain in all of the models, but the morphology is affected for the $7M_{\odot}$ model. In the case of $M_{\rm S}=2$ TeV, the loop is eliminated for the $10M_{\odot}$ and $9M_{\odot}$ stars. When $M_{\rm S}=1$ TeV, the blue loops are eliminated for all of the models.

 $^{^{7}}$ Models heavier than $10 M_{\odot}$ do not undergo the blue loops with the adopted parameters.

As noted in Section 1, these values of the magnetic moment are in the range explored in the reactor experiments, but higher than the limit inferred from globular clusters.

⁹ These values are smaller than those inferred from collider experiments and low-mass stars, but they correspond to the size of compactified dimension currently explored in the torsion balance experiments.

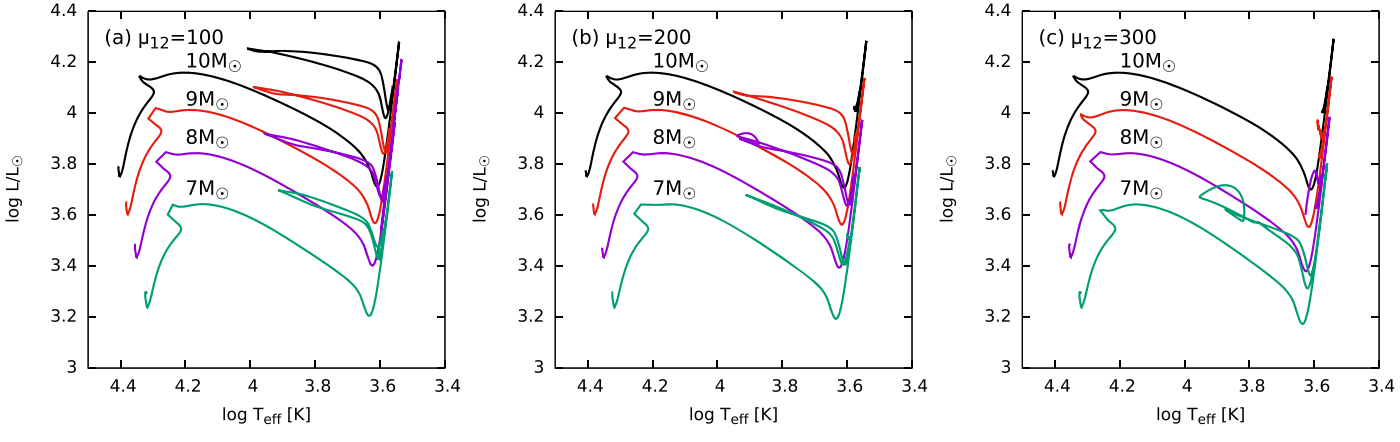


Figure 2. H-R diagram with the NMMs of (a) $\mu_{12} = 100$, (b) $\mu_{12} = 200$, and (c) $\mu_{12} = 300$ in Case A.

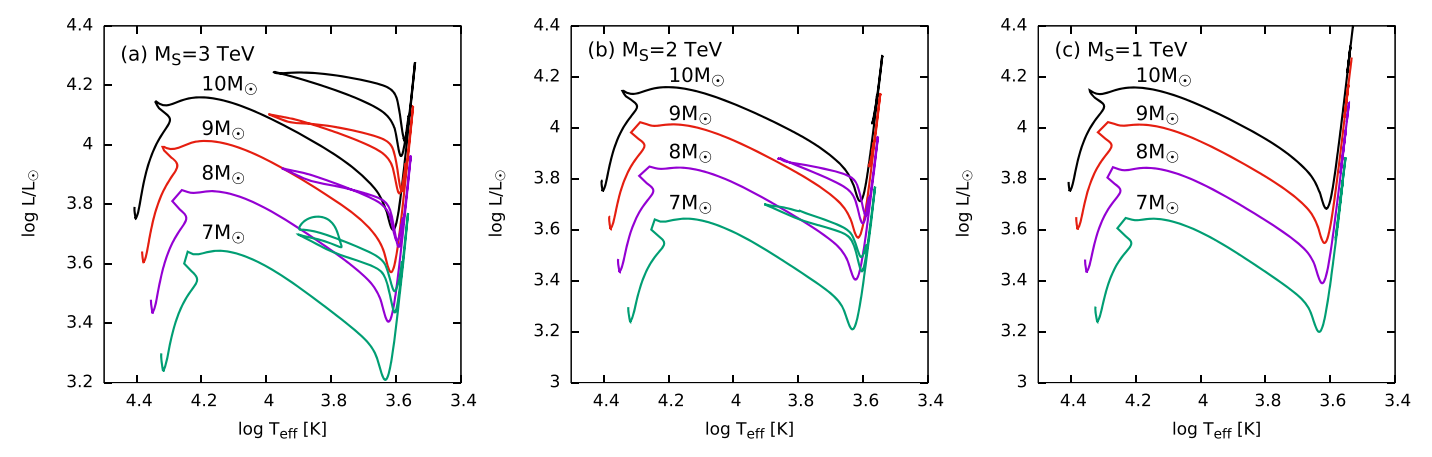


Figure 3. H-R diagram with LED of (a) $M_S = 3$ TeV, (b) $M_S = 2$ TeV, and (c) $M_S = 1$ TeV in Case A.

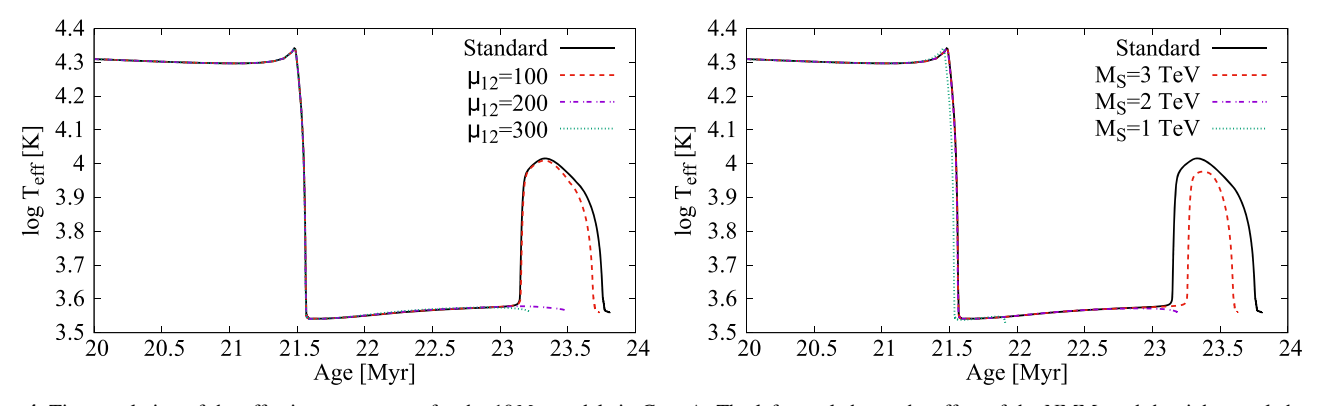


Figure 4. Time evolution of the effective temperature for the $10M_{\odot}$ models in Case A. The left panel shows the effect of the NMM, and the right panel shows the effect of LED.

Although the blue loops do not disappear for $\mu_{12}=100$ and $M_{\rm S}=3$ TeV, the duration, $t_{\rm BG}$, of the blue giant phase becomes shorter because of the additional energy loss. Figure 4 shows the evolution of the effective temperature as a function of the stellar age for these cases. The left panel shows the result for various assumptions of the NMM, and the right panel shows the result for various assumptions of LED sizes. The sudden expansion at ~21.5 Myr is the Hertzsprung gap, where the helium core contracts rapidly and the envelope expands (Sandage & Schwarzschild 1952; Kippenhahn et al. 2012). The bump around ~23.5 Myr corresponds to the blue loop. It is seen that $t_{\rm BG}=0$. 64 Myr in the standard case, while $t_{\rm BG}=0$. 55 Myr when $\mu_{12}=100$ and $t_{\rm BG}=0$. 35 Myr when $M_{\rm S}=3$

TeV. This difference is potentially observable from the ratio of blue and red giants (Dohm-Palmer & Skillman 2002; McQuinn et al. 2011).

3.1.2. Case B

The H-R diagram in the standard case is shown in the bottom panel of Figure 1. The blue loops appear in all of the models with $7-10M_{\odot}$. The edges of the blue loops are bluer than those in Case Δ

Figure 5 is the H-R diagram with NMMs of $\mu_{12} = 100$, 200, and 300. The blue loops remain in the case of $\mu_{12} = 100$, while

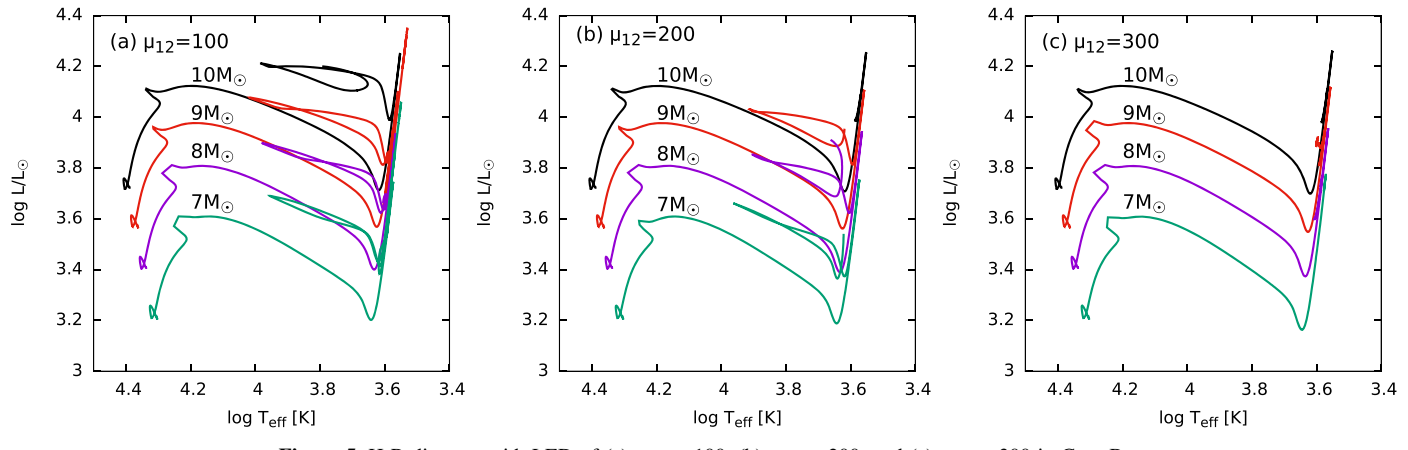


Figure 5. H-R diagram with LED of (a) $\mu_{12} = 100$, (b) $\mu_{12} = 200$, and (c) $\mu_{12} = 300$ in Case B.

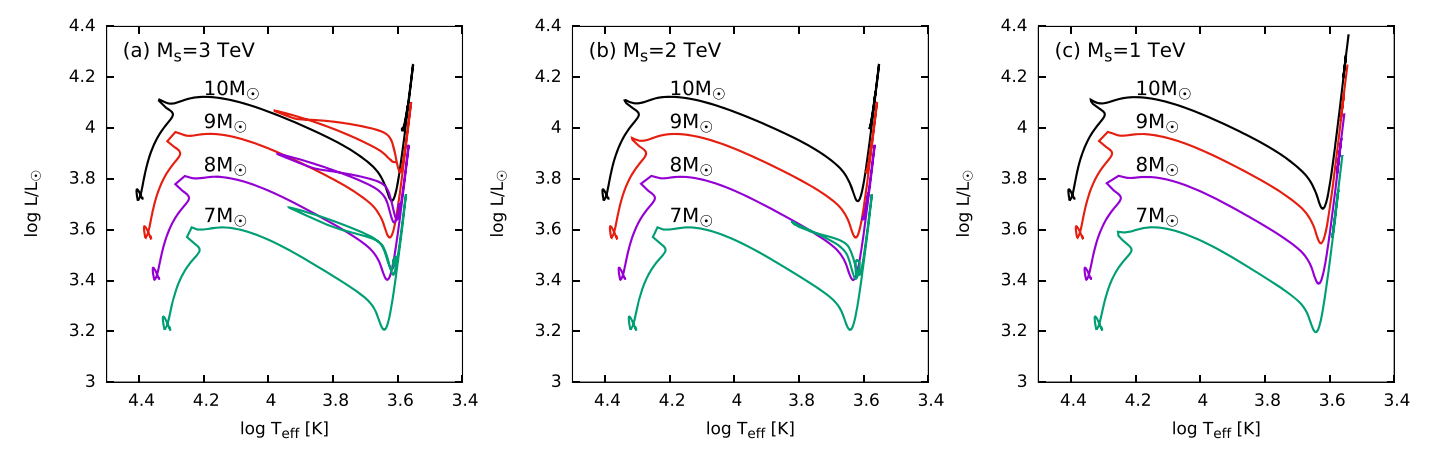


Figure 6. H-R diagram with LED of (a) $M_S = 3$ TeV, (b) $M_S = 2$ TeV, and (c) $M_S = 1$ TeV in Case B.

they are eliminated in the $10M_{\odot}$ model when $\mu_{12}=200$ and in all of the 7, 8, 9, and $10M_{\odot}$ models when $\mu_{12}=300$.

Figure 6 is the H-R diagram with LEDs of $M_S = 3$, 2, and 1 TeV. Contrary to the result in Case A, the blue loop in the $10M_{\odot}$ model is eliminated even when $M_S = 1$ TeV. Only the blue loop in the $7M_{\odot}$ model survives when $M_S = 2$ TeV, and all of the loops are eliminated when $M_S = 3$ TeV.

3.2. Evolution of the Core

Figure 7 shows the central temperature and density evolution for stars of various masses. The top panel shows the result with an assumed NMM of $\mu_{12} = 200$, and the bottom panel shows the result with an LED of $M_{\rm S} = 2$ TeV. The gray contour shows the enhancement factor, $\log f$, of the energy loss defined as

$$\log f = \log \left(\frac{\epsilon_{\nu} + \epsilon_{\text{extra}}}{\epsilon_{\nu}} \right), \tag{10}$$

where ϵ_{ν} is the standard energy loss and $\epsilon_{\rm extra}$ is the additional energy loss caused by the NMM of $\mu_{12}=200$ and LED of $M_{\rm S}=2$ TeV. It is seen that the energy-loss rate is enhanced by 10^2-10^4 times.

From Figure 7, one sees that the contribution of $\epsilon_{\rm extra}$ decreases as a function of the temperature when $\mu_{12}=200$, while it increases when $M_{\rm S}=2$ TeV. This is explained in Figure 8, which shows the energy-loss rates of each elementary process at a density of 10^4 g cm⁻³. The top panel assumes an

NMM of $\mu_{12}=200$, and the bottom panel assumes an LED of $M_{\rm S}=2$ TeV. Here $\epsilon_{\rm plas}^{\,\mu}$, $\epsilon_{\rm pair}^{\,\mu}$, $\epsilon_{\gamma\gamma}$, $\epsilon_{\rm GCP}$, and $\epsilon_{\rm GB}$ are defined in Section 2. The values of $\epsilon_{\rm tot}^{\,\mu}$ and $\epsilon_{\rm tot}^{\,\rm KK}$ are the total energy loss due to the NMM and LED, respectively. The values $\epsilon_{\rm pair}$, $\epsilon_{\rm plas}$, and $\epsilon_{\rm tot}$ are the standard neutrino energy losses (Itoh et al. 1996). In the case of $\mu_{12}=200$, the dominant process at log $T\sim 8.2$, where helium burning occurs, is plasmon decay. On the other hand, in the case of $M_{\rm S}=2$ TeV, the dominant process is photon–photon annihilation. The photoneutrino energy-loss rate $\epsilon_{\rm photo}$ is proportional to T^{8} (Petrosian et al. 1967), while the plasma energy-loss rate $\epsilon_{\rm plas}^{\,\mu}$ is proportional to T^{3} (Inman & Ruderman 1964). This is the reason why f becomes smaller in the hot region when $\mu_{12}=200$. On the other hand, the photon–photon annihilation rate $\epsilon_{\gamma\gamma}$ is proportional to T^{9} (Barger et al. 1999); therefore, f is larger in the hot region when $M_{\rm S}=2$.

The physical mechanism at the onset of the blue loops is still under debate (e.g., Xu & Li 2004a; Kippenhahn et al. 2012). One possible mechanism is the so-called mirror reflection principle. When a star leaves the red giant branch to the blue loop, nuclear burning energy is used to expand the core (Choplin et al. 2017). Because of the mirror reflection principle, the expansion of the core leads to the contraction of the envelope and thus higher effective temperature. However, the NMM and LED extract energy from the core and prevent the expansion of the core. Therefore, a star cannot start a detour to a blue giant.

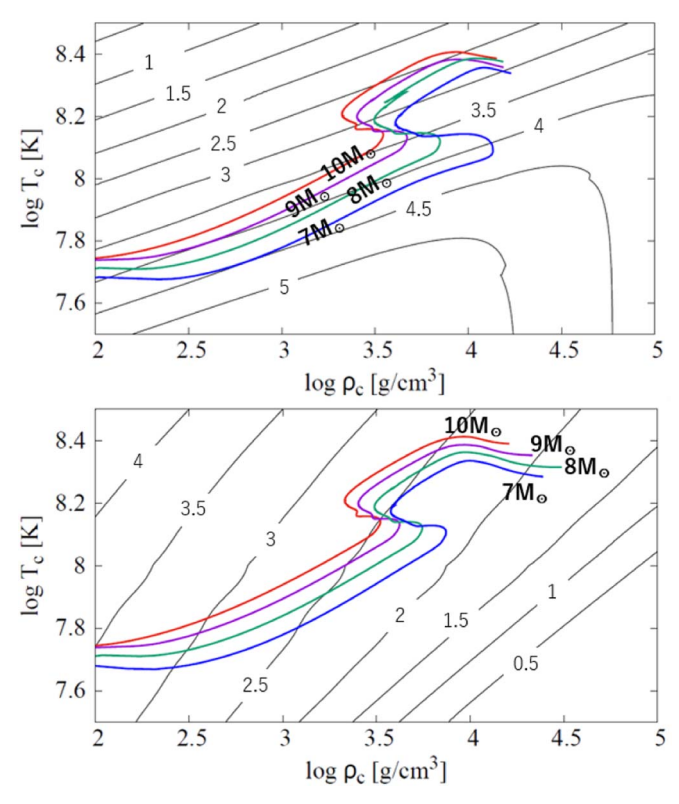


Figure 7. Evolution of the central temperature and density in Case A. The top panel shows the effect of the NMM of $\mu_{12}=200$, and the bottom panel shows the effect of an LED of $M_{\rm S}=2$ TeV. The contour shows the enhancement factor $\log f$ defined in the text.

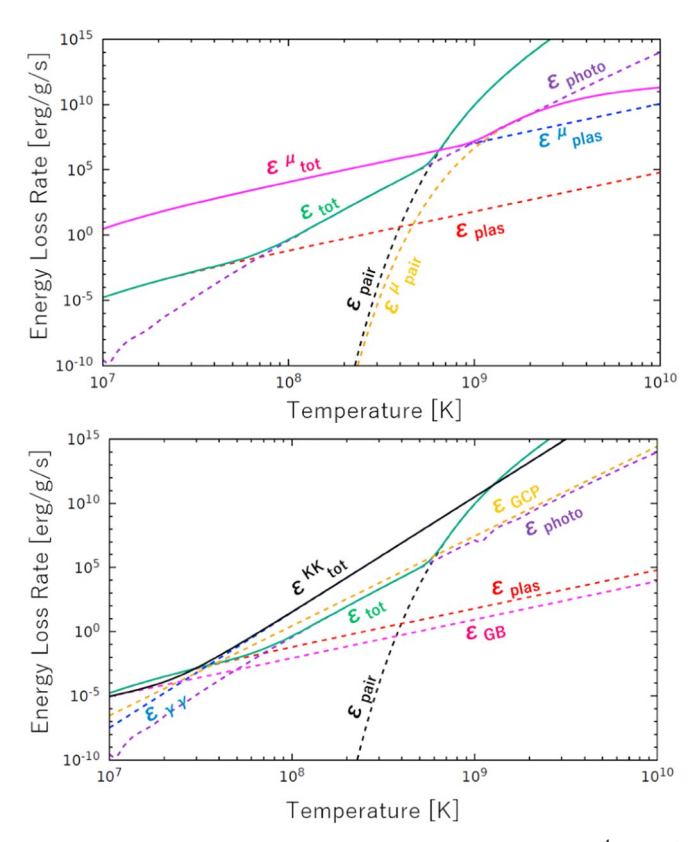


Figure 8. Different contributions to the energy-loss rates at $\rho = 10^4$ g cm⁻³. The top panel shows the effect of the NMM of $\mu_{12} = 200$, and the bottom panel shows the effect of an LED of $M_{\rm S} = 2$ TeV.

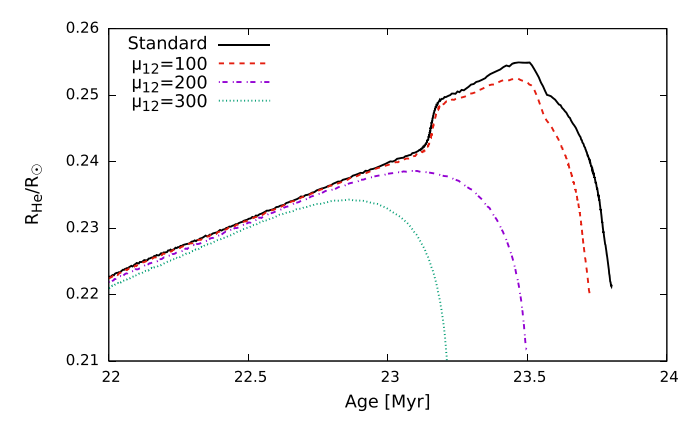


Figure 9. Radii of the helium core as a function of stellar age for the $10M_{\odot}$ models in Case A. The solid line shows the result without the NMM, and the others show the results for $\mu_{12}=100,\,200,\,$ and 300.

Figure 9 shows the evolution of the helium core radius with different NMMs. It is seen that the core radius $R_{\rm He}$ increases after \sim 23.2 Myr in the case of $\mu_{12}=0$ and 100, while it decreases when $\mu_{12}=200$ and 300. This is consistent with the explanation of the blue loop by the mirror reflection principle.

3.3. Effects of Reaction Rate Uncertainties

In the fiducial models, we adopt the NACRE reaction rates (Angulo et al. 1999). However, uncertainties in nuclear reaction rates can significantly affect morphology of the blue loops (Brunish & Becker 1990; Xu & Li 2004a; Valle et al. 2009) and thus the threshold of elimination of the loops. In this section, we study the effects of uncertainties in the triple- α and 12 C (α , γ) 16 O reactions, which govern core helium burning.

3.3.1. Triple-\alpha Reaction

NACRE estimates temperature-dependent uncertainties in the triple- α reaction to be $\lesssim 20\%$ at $\sim 10^8$ K. We adopt these uncertainties to study the sensitivity of the blue loops.

Figure 10 shows the evolution of the $10M_{\odot}$ star with the triple- α reactions changed within the NACRE uncertainties. Although the loop extends to the slightly bluer region when the lower rate is adopted, morphology of the blue loops is not affected significantly by the different triple- α rates. This suggests that the threshold of elimination of the loops is robust against the present uncertainties.

3.3.2.
$$^{12}C$$
 $(\alpha, \gamma)^{16}O$ Reaction

The low-energy cross sections of the 12 C (α , γ) 16 O reaction have not been measured yet (e.g., deBoer et al. 2017). Kunz et al. (2002) proposed lower reaction rates than the NACRE compilation, based on their new measurements of E1- and E2-capture cross sections. Their reaction rates are $\sim\!\!30\%$ smaller than the NACRE rate at $\sim\!\!10^8$ K. We adopt the rate recommended by Kunz et al. (2002) to perform a sensitivity study.

Figure 11 shows the evolution of the $10M_{\odot}$ model with the different $^{12}\mathrm{C}$ (α , γ) $^{16}\mathrm{O}$ reaction rates. It is seen that the tip of the blue loop becomes redder when the Kunz et al. (2002) rate is adopted and the shape of the loops is significantly different around $\log T_{\rm eff} \sim 3.65$ between the two.

Figure 12 shows the evolution of the $7-10M_{\odot}$ stars with the 12 C $(\alpha, \gamma)^{16}$ O rate quoted in Kunz et al. (2002). When

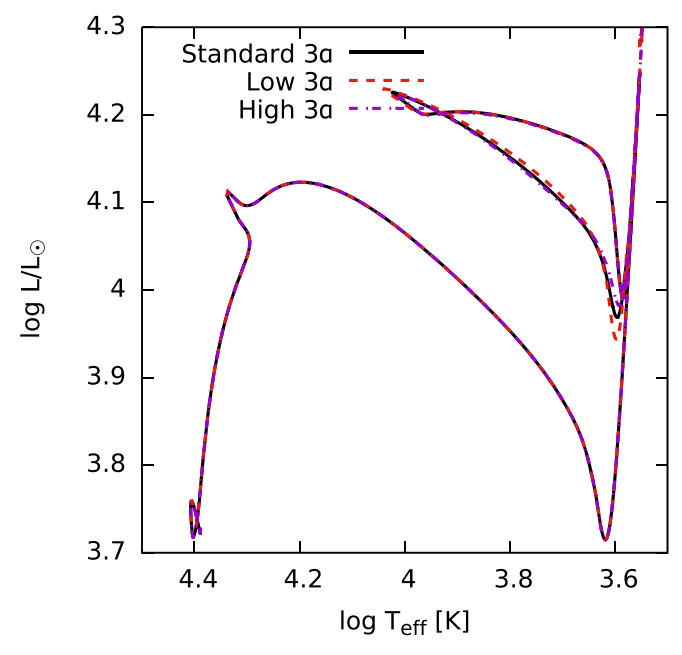


Figure 10. H-R diagram of the $10M_{\odot}$ model with different triple- α reaction rates. The solid line adopts the NACRE standard reaction rate, while the dashed lines adopt the higher and lower limits of the rate quoted in the NACRE table. The initial composition is set to be Case B.

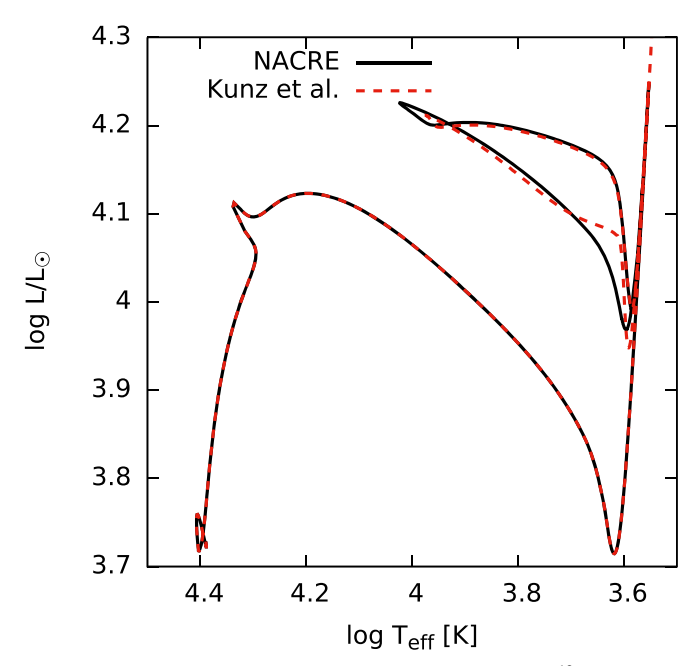


Figure 11. H-R diagram of the $10M_{\odot}$ model with different 12 C $(\alpha, \gamma)^{16}$ O reaction rates. The solid line adopts the NACRE standard reaction rate, while the dashed line adopts the rate quoted in Kunz et al. (2002). The initial composition is set to be Case B.

beyond-standard physics is not adopted, the tip of the blue loops becomes redder when reaction rate is lower, as reported in Valle et al. (2009) and Brunish & Becker (1990). Interestingly, the threshold of elimination of the loops is much lower than that with the NACRE rate. As shown in Figure 12, the blue loops are suppressed in the $10M_{\odot}$ model when $\mu_{12} > 40$ or $M_{\rm S} < 5$ TeV with the rate in Kunz et al. (2002), while these thresholds are $\mu_{12} > 200$ and $M_{\rm S} < 3$ TeV for the NACRE rate, respectively, as has already been discussed in Figures 2–6.

3.4. Effects on Heavier Cepheids

Some of Galactic Cepheid progenitors have been estimated (Turner 1996) to be as massive as $\sim 20 M_{\odot}$, using an empirical mass–period relation of Cepheids. Models of such a massive star do not undergo the blue loop during central helium burning (e.g., Schaller et al. 1992; Bono et al. 2000; Valle et al. 2009; Anderson et al. 2016). Less massive stars with $<15 M_{\odot}$ cross the Hertzsprung gap so rapidly that there is little chance to observe those in the instability strip. However, massive stars with $>15 M_{\odot}$ achieve a central temperature high enough to ignite helium burning before they reach the red giant branch. In this case, the time to cross the gap slows down, so it becomes more probable to observe them in the instability strip.

Figure 13 shows evolution of the effective temperature for the $20M_{\odot}$ models in Case B. The black line shows the standard evolution, and the purple and red lines adopt $\mu_{12}=100$ and $M_{\rm S}=3$ TeV, respectively. It is seen that the extra energy losses shorten the timescale of helium burning. The circles show crossing of the blue edge of the instability strip. Although validity of the extrapolation of the model edge (Bono et al. 2000) to higher luminosities is uncertain, the stars spend 10–20 kyr in the instability strip even when $\mu_{12}=100$ or $M_{\rm S}=3$ TeV is adopted. Therefore, these effects do not contradict the observed rare massive Cepheids.

3.5. Possible Effects of Mass Loss and Rotation

The purpose of this paper is to show fiducial models of intermediate-mass stars with physics beyond the SM, so exhaustive evaluation of theoretical uncertainties is out of its scope. However, the evolution of intermediate-mass stars is sensitive to other physical processes, which is the very reason why they can potentially be used as a probe of new physics.

In our models, the treatment of mass loss in the red supergiant phase and the blue loop is based on de Jager et al. (1988), which covers the temperature and the luminosity ranges we are interested in. This mass-loss rate on the main sequence (MS) is not considered because it is as small as 10^{-8} – $10^{-9}M_{\odot}$ yr⁻¹ (de Jager et al. 1988). Figure 14 shows the comparison between the $10M_{\odot}$ models with and without mass loss during the MS. The solid line shows the fiducial model, which was also shown in Figure 1, and the dashed line shows the model with the additional mass loss based on de Jager et al. (1988). It is seen that the mass loss during the MS slightly decreases the luminosity of the blue loop. The effect of the mass loss on the MS on morphology of the blue loops is moderate and thus is not a major source of uncertainties.

It has been pointed out that shocks generated by the pulsation drive mass loss up to $10^{-7} M_{\odot} \, \mathrm{yr}^{-1}$ (Neilson & Lester 2008). Because of such pulsation-driven mass loss, Cepheid variables can lose 5%–10% of their mass (Neilson et al. 2011). Morphology of the blue loops can be significantly affected by pulsation-driven mass loss, so it is desirable to study uncertainties that originate from it.

Effects of rotation are not included in our models. However, the typical rotational velocity of B stars on the MS with $5-9M_{\odot}$ is as high as 10%-30% of the critical velocity (Huang et al. 2010), so it is important to study the rotational effect. Rotation makes the blue loops more luminous systematically and affects the mass–luminosity relation of Cepheids (Ekström et al. 2012; Anderson et al. 2016).

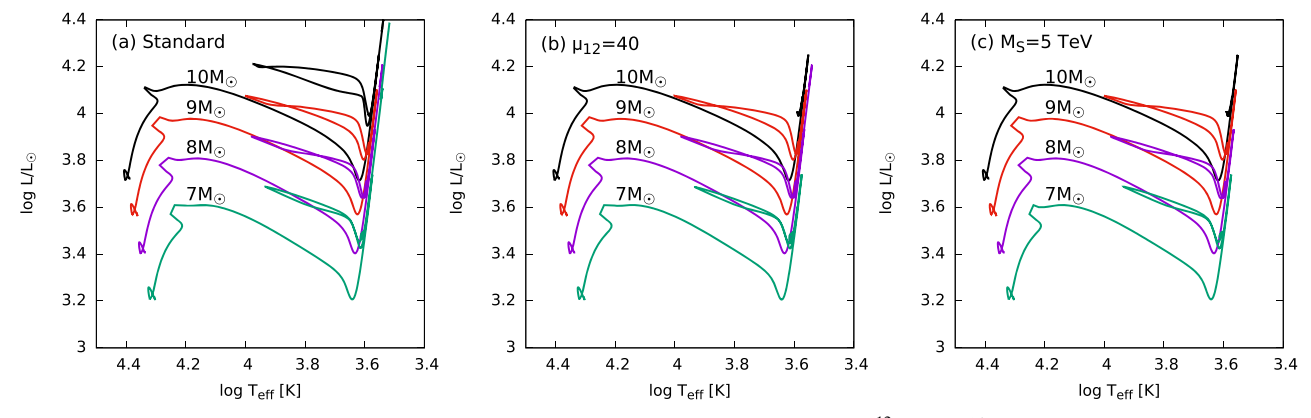


Figure 12. H-R diagram (a) without beyond SM physics, (b) with $\mu_{12}=40$, and (c) with $M_{\rm S}=5$ TeV. The $^{12}{\rm C}$ ($\alpha,~\gamma$) $^{16}{\rm O}$ rate is from Kunz et al. (2002). The initial composition is set to be Case B.

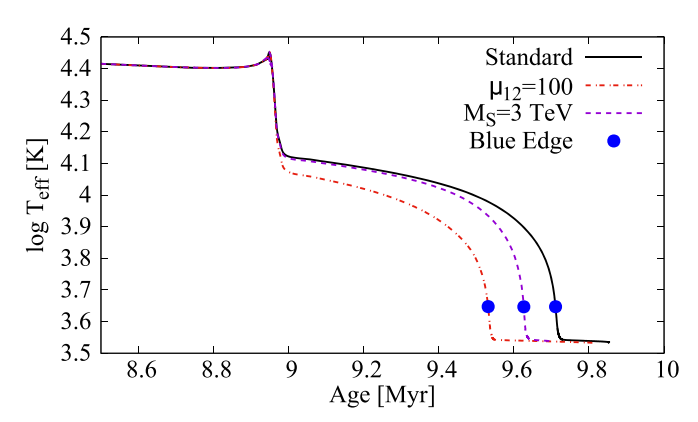


Figure 13. Time evolution of the effective temperature for the $20M_{\odot}$ models in Case B. The black line shows the SM, and the purple and red lines adopt $\mu_{12}=100$ and $M_{\rm S}=3$ TeV, respectively. The circles represent crossing of the blue edge of the instability strip (Bono et al. 2000).

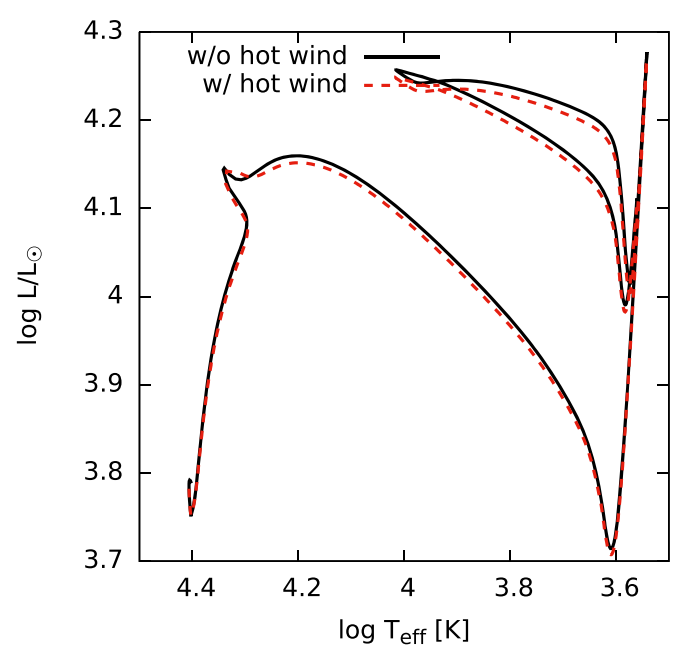


Figure 14. H-R diagram for the $10M_{\odot}$ models with standard physics in Case A. The solid line shows the model without mass loss on the MS, while the dashed line shows the model with it.

4. Conclusions

In this paper, we studied the effect of the NMM and LED on the evolution of intermediate-mass stars. We find that the blue loops are eliminated unless $\mu_{12} < 200$ or $M_{\rm S} > 2$ TeV, placing observational limits on μ_{12} and $M_{\rm S}$. In our models, $10M_{\odot}$ stars are the most sensitive to beyond-standard physics.

From Figure 1, it is seen that the luminosity of $10M_{\odot}$ Cepheids is $\log L/L_{\odot} \sim 4.2$. The period–luminosity relation of Cepheids is written as (Cox 1980)

$$\log\left(\frac{L}{L_{\odot}}\right) = 1.15\log\left(\frac{P}{1\text{ day}}\right) + 2.47,\tag{11}$$

where P is the pulsation period. Putting $\log L/L_{\odot} \sim 4.2$ into this formula, we get $P \sim 32$ days. Cepheids with this period are observed in the Galaxy (Turner 1996; Berdnikov et al. 2000; Sandage & Tammann 2006). The existence of $10M_{\odot}$ Cepheids places an independent constraint on the NMM and LEDs.

The current constraints that come from ground experiments are $\mu_{12} < 29$ (Beda et al. 2013). Depending on the $^{12}\mathrm{C}$ (α, γ) $^{16}\mathrm{O}$ rate, our constraint on the NMM is either somewhat weaker or comparable to the experimental limit, but higher than the limit inferred from globular clusters.

Using Equation (1), the lower limit on $M_{\rm S}$ is transformed to an upper limit R < 30–170 $\mu{\rm m}$ compared to the result $R < 30~\mu{\rm m}$ reported by the torsion experiment (Lee et al. 2020). Equation (3) shows that the constraint $M_{\rm D} > 9.9~{\rm TeV}$, which was reported by the CMS experiment (Sirunyan et al. 2018), is equivalent to an upper limit of $R < 24~\mu{\rm m}$. This is to be compared with our result of $M_{\rm S} > 2~{\rm to}~5~{\rm TeV}$. The fundamental scale value we constrain corresponds to the size of the compactified dimensions comparable to those explored in the torsion balance experiments, but it is smaller than the limits inferred from collider experiments and low-mass stars. In the above results the range depends on the input values of both the $^{12}{\rm C}~(\alpha, \gamma)^{16}{\rm O}$ rate and the metallicity.

In this study, we focused on the n=2 case. We also performed calculations with n=3 extra dimensions, using formulae shown in Cassisi et al. (2000) and Barger et al. (1999). It is found that the blue loop of a $10M_{\odot}$ star is eliminated when $M_{\rm S} \leqslant 60$ GeV. Therefore, the mass scale for the n=3 case can be constrained to be $M_{\rm S} > 60$ GeV. The

CMS experiment (Sirunyan et al. 2018), on the other hand, reports $M_{\rm D} > 7.5$ TeV, so collider experiments can achieve much tighter constraints than energy-loss arguments do in the n=3 case.

More quantitative constraints could be achieved by arguments on the timescale of stellar evolution. We saw that the duration of blue giants is shorter when the NMM or LED is included. In order to compare the results with observations, it is desirable to draw isochrones and to superpose them on the color–magnitude diagram. To do so, one must perform calculations with finer grids of stellar masses. The quantitative approach can potentially tighten the constraints on the NMM and LED, but this is beyond the scope of this paper.

The morphology of the blue loops is very sensitive to input physics including nuclear reaction rates and treatment of metallicity (Xu & Li 2004a, 2004b; Valle et al. 2009; Morel et al. 2010; Suda et al. 2011; Halabi et al. 2012). Our results show that there are theoretical uncertainties that originate from these ingredients. To tighten the bounds we obtained, it is desirable to perform systematic studies on the effects of different input physics on the constraints of beyond-standard physics.

The authors would like to thank Wako Aoki and Hirokazu Sasaki for fruitful discussions. K.M. is supported by JSPS KAKENHI grant No. JP19J12892. T.K. is supported in part by Grants-in-Aid for Scientific Research of JSPS (17K05459, 20K03958). M.K. is supported by the NSFC Research Fund for International Young Scientists (11850410441). A.B.B. is supported in part by the U.S. National Science Foundation grant No. PHY-1806368. M.A.F. is supported by National Science Foundation grant No. PHY-1712832 and by NASA grant No. 80NSSC20K0498. M.A.F. and A.B.B. acknowledge support from the NAOJ Visiting Professor program.

Software: MESA (Paxton et al. 2011, 2013, 2015, 2018, 2019).

ORCID iDs

References

```
Aaboud, M., Aad, G., Abbott, B., et al. 2018, JHEP, 2018, 126
Adelberger, E. G., Gundlach, J. H., Heckel, B. R., et al. 2009, PrPNP, 62, 102
Alastuey, A., & Jancovici, B. 1978, ApJ, 226, 1034
Anders, E., & Grevesse, N. 1989, GeoCoA, 53, 197
Anderson, R. I., Saio, H., Ekström, S., et al. 2016, A&A, 591, A8
Angulo, C., Arnould, M., Rayet, M., et al. 1999, NuPhA, 656, 3
Antoniadis, I., Arkani-Hamed, N., Dimopoulos, S., & Dvali, G. 1998, PhLB, 436, 257
Arceo-Díaz, S., Schröder, K.-P., Zuber, K., et al. 2015, APh, 70, 1
Arkani-Hamed, N., Dimopoulos, S., & Dvali, G. 1998, PhLB, 429, 263
Asplund, M., Grevesse, N., & Sauval, A. J. 2005, in ASP Conf. Ser., Cosmic Abundances as Records of Stellar Evolution and Nucleosynthesis, ed. T. G. Barnes, III & F. N. Bash (San Francisco, CA: ASP), 25
Asplund, M., Grevesse, N., Sauval, A. J., et al. 2009, ARA&A, 47, 481
Balantekin, A. B., & Kayser, B. 2018, ARNPS, 68, 313
Barger, V., Han, T., Kao, C., et al. 1999, PhLB, 461, 34
```

```
Beda, A. G., Brudanin, V. B., Egorov, V. G., et al. 2013, PPNL, 10, 139
Berdnikov, L. N., Dambis, A. K., & Vozyakova, O. V. 2000, A&AS, 143, 211
Bono, G., Caputo, F., Cassisi, S., et al. 2000, ApJ, 543, 955
Bono, G., Castellani, V., & Marconi, M. 2000, ApJ, 529, 293
Brunish, W. M., & Becker, S. A. 1990, ApJ, 351, 258
Cassisi, S., Castellani, V., Degl'Innocenti, S., et al. 2000, PhLB, 481, 323
Choplin, A., Coc, A., Meynet, G., et al. 2017, A&A, 605, A106
Cox, J. P. 1980, Theory of Stellar Pulsation (Princeton, NJ: Princeton Univ.
de Jager, C., Nieuwenhuijzen, H., & van der Hucht, K. A. 1988, A&AS,
deBoer, R. J., Görres, J., Wiescher, M., et al. 2017, RvMP, 89, 035007
Dohm-Palmer, R. C., & Skillman, E. D. 2002, AJ, 123, 1433
Ekström, S., Georgy, C., Eggenberger, P., et al. 2012, A&A, 537, A146
Evans, N. R. 1993, AJ, 105, 1956
Ferguson, J. W., Alexander, D. R., Allard, F., et al. 2005, ApJ, 623, 585
Fermi-LAT Collaboration, Ajello, M., Baldini, L., et al. 2012, JCAP, 2012, 012
Friedland, A., Giannotti, M., & Wise, M. 2013, PhRvL, 110, 061101
Fujikawa, K., & Shrock, R. E. 1980, PhRvL, 45, 963
Fukuda, Y., Hayakawa, T., Ichihara, E., et al. 1998, PhRvL, 81, 1562 Fuller, G. M., Fowler, W. A., & Newman, M. J. 1985, ApJ, 293, 1
Giunti, C., & Studenikin, A. 2015, RvMP, 87, 531
Haft, M., Raffelt, G., & Weiss, A. 1994, ApJ, 425, 222
Halabi, G. M., El Eid, M. F., & Champagne, A. 2012, ApJ, 761, 10
Hannestad, S., & Raffelt, G. G. 2003, PhRvD, 67, 125008
Hansen, B. M. S., Richer, H., Kalirai, J., et al. 2015, ApJ, 809, 141
Heger, A., Friedland, A., Giannotti, M., et al. 2009, ApJ, 696, 608
Huang, W., Gies, D. R., & McSwain, M. V. 2010, ApJ, 722, 605
Iglesias, C. A., & Rogers, F. J. 1993, ApJ, 412, 752
Iglesias, C. A., & Rogers, F. J. 1996, ApJ, 464, 943
Inman, C. L., & Ruderman, M. A. 1964, ApJ, 140, 1025
Itoh, N., Hayashi, H., Nishikawa, A., et al. 1996, ApJS, 102, 411
Itoh, N., Totsuji, H., Ichimaru, S., & Dewitt, H. E. 1979, ApJ, 234, 1079
Kippenhahn, R., Weigert, A., & Weiss, A. 2012, Stellar Structure and
   Evolution (Berlin: Springer)
Kunz, R., Fey, M., Jaeger, M., et al. 2002, ApJ, 567, 643
Langanke, K., & Martínez-Pinedo, G. 2000, NuPhA, 673, 481
Lee, J. G., Adelberger, E. G., Cook, T. S., et al. 2020, PhRvL, 124, 101101
Lodders, K. 2020, Solar Elemental Abundances, in The Oxford Research
   Encyclopedia of Planetary Science (Oxford: Oxford Univ. Press)
McQuinn, K. B. W., Skillman, E. D., Dalcanton, J. J., et al. 2011, ApJ, 740, 48
Morel, P., Provost, J., Pichon, B., et al. 2010, A&A, 520, A41
Murata, J., & Tanaka, S. 2015, CQGra, 32, 033001
Neilson, H. R., Cantiello, M., & Langer, N. 2011, A&A, 529, L9
Neilson, H. R., & Lester, J. B. 2008, ApJ, 684, 569
Oda, T., Hino, M., Muto, K., Takahara, M., & Sato, K. 1994, ADNDT, 56, 231
Paxton, B., Bildsten, L., Dotter, A., et al. 2011, ApJS, 192, 3
Paxton, B., Cantiello, M., Arras, P., et al. 2013, ApJS, 208, 4
Paxton, B., Marchant, P., Schwab, J., et al. 2015, ApJS, 220, 15
Paxton, B., Schwab, J., Bauer, E. B., et al. 2018, ApJS, 234, 34
Paxton, B., Smolec, R., Schwab, J., et al. 2019, ApJS, 243, 10
Petrosian, V., Beaudet, G., & Salpeter, E. E. 1967, PhRv, 154, 1445
Raffelt, G., & Weiss, A. 1992, A&A, 264, 536
Raffelt, G. G. 1996, Stars as Laboratories for Fundamental Physics: The
   Astrophysics of Neutrinos (Chicago, IL: Univ. Chicago Press)
Rogers, F. J., & Nayfonov, A. 2002, ApJ, 576, 1064
Sandage, A., & Tammann, G. A. 2006, ARA&A, 44, 93
Sandage, A. R., & Schwarzschild, M. 1952, ApJ, 116, 463
Schaller, G., Schaerer, D., Meynet, G., et al. 1992, A&AS, 96, 269
Shrock, R. E. 1982, NuPhB, 206, 359
Sirunyan, A. M., Tumasyan, A., Adam, W., et al. 2018, PhRvD, 97, 092005
Suda, T., Hirschi, R., & Fujimoto, M. Y. 2011, ApJ, 741, 61
Tan, W.-H., Du, A.-B., Dong, W.-C., et al. 2020, PhRvL, 124, 051301
Tanabashi, M., Hagiwara, K., Hikasa, K., et al. 2018, PhRvD, 98, 030001
Timmes, F. X., & Swesty, F. D. 2000, ApJS, 126, 501
Turner, D. G. 1996, JRASC, 90, 82
Turner, D. G., & Burke, J. F. 2002, AJ, 124, 2931
Valle, G., Marconi, M., Degl'Innocenti, S., et al. 2009, A&A, 507, 1541
Viaux, N., Catelan, M., Stetson, P. B., et al. 2013a, A&A, 558, A12
Viaux, N., Catelan, M., Stetson, P. B., et al. 2013b, PhRvL, 111, 231301
Xu, H. Y., & Li, Y. 2004a, A&A, 418, 213
Xu, H. Y., & Li, Y. 2004b, A&A, 418, 225
```